

Strain-induced Ferroelectricity and Bulk Photovoltaic Effect in One-dimensional Antiferromagnetic WOI_3

Zhihao Gong^{1#}, Yechen Xun^{2#}, Zhuang Qian³, Kai Chang¹, Jingshan Qi^{4*}, Hua Wang^{1*}

¹ZJU-Hangzhou Global Scientific and Technological Innovation Center, School of Physics, Zhejiang University, Hangzhou 311215, China

²Department of Physics and Astronomy, The University of Tennessee, Knoxville, Tennessee 37996, USA

³Institute of Natural Sciences, Westlake Institute for Advanced Study, Hangzhou, Zhejiang 810024, China

⁴Tianjin Key Laboratory of Quantum Optics and Intelligent Photonics, School of Science, Tianjin University of Technology, Tianjin 300384, China

*Correspondence to: qijingshan@email.tjut.edu.cn, daodaohw@zju.edu.cn

Abstract

The pursuit of multiferroic magnetoelectrics, combining simultaneous ferroelectric and magnetic orders, remains a central focus in condensed matter physics. Here we report the centrosymmetric, one-dimensional (1D) antiferromagnetic WOI_3 undergoes a strain-induced ferroelectric distortion. The paraelectric-ferroelectric transition is originated from the unconventional anisotropic d^1 mechanism, where an unpaired d electron of each W^{5+} ion contributes to magnetic orders. Employing a Heisenberg model with Dzyaloshinskii–Moriya interaction, we predict an antiferromagnetic spin configuration as the paraelectric ground state, transitioning to a ferroelectric phase with noncollinear spin arrangement under uniaxial strain. The ferroelectric polarization and noncollinear spin arrangement can be manipulated by varying the applied strain. While the energy barriers for switching ferroelectric polarizations with magnetic orders are on the order of a few dozen of meV, the shift current bulk photovoltaic effect (BPVE) exhibits remarkable differences, providing a precise and valuable tool for experimentally probing the interplay of ferroelectric and magnetic orders in 1D WOI_3 .

Key words: Ferroelectricity, antiferromagnetism, bulk photovoltaic effect, shift current, one-dimensional material, strain engineering, first-principles calculation

Multiferroics have been a focal point in the realm of condensed matter physics^{1–6}, and are promising to be vastly applied in nonvolatile data storage, sensors, actuators and so on⁶, especially for those materials combining ferroelectricity (FE) and magnetic behaviors⁴. Due to clean surfaces and large dielectric constant in miniaturization of the electronic devices⁶, low-dimensional (1D-, 2D-) multiferroic materials have attracted significant attentions for these days. Based on the mechanism of generating multiferroicity^{2,5}, multiferroic materials can be classified into Type-I (sources of FE and magnetism are independent) and Type-II (magnetism causes FE) categories. Notable examples of Type-I materials include artificial low-dimensional materials, like halogen-decorated phosphorene bilayers⁷, 2D Van der Waals (vdW) heterostructure of Cr₂Ge₂Te₆ onto In₂Se₃⁸, etc. and transition-metal halide monolayers, like (CrBr₃)₂Li⁹, while Hf₂VC₂F₂ MXene Monolayer¹⁰ and few-layer NiI₂¹¹ belong to Type-II.

Type-I multiferroic materials violating the conventional d^0 rule of octahedral distortion for FE by external strain engineering^{12,13}, and intrinsic anisotropic d^1 rule^{14–16} provide the potential for simultaneous magnetic and ferroelectric ordering. Increasing the lattice constants, epitaxial strains and chemical pressure are discussed in stabilizing the FE state in antiferromagnetic (AFM) materials like SrMnO₃¹² and BaMnO₃¹³, respectively. On the other side, the materials of d^1 configurations, if governed by Hund's rule, exhibit no pseudo Jahn-Teller effect (PJTE) on dipolar distortion and no ferroelectric instability^{17,18}, due to the mismatch in spin multiplicities of the lowest unoccupied molecular orbital (LUMO) and the highest occupied molecular orbital (HOMO). Nevertheless, d^1 configurations haven't been fully excluded from satisfying the condition of PJTE¹⁸. The anisotropic d^1 rule is recently proposed in predicting the ground-state FE and AFM orders in the 2D VOX₂ (X=Br, Cl, I) monolayer¹⁴. Additionally, the spiral-spin noncollinear magnetic order is then predicted by introducing the effect of the Dzyaloshinskii–Moriya interaction (DMI)¹⁶.

In this work, we report the strain-induced coexistence of ferroelectricity and antiferromagnetism of the 1D vdW semiconductor WOI₃ based on density functional theory (DFT) calculations. Distinct from the recently reported octahedral quasi-1D WOX₄¹⁹ and 1D WOF₄²⁰, in which the intrinsic ferroelectricity is rooted from the electronic d^0 configurations, the 1D WOI₃ material exhibits anisotropic d^1 configuration despite sharing similar octahedral structures, and is predicted to experience a paraelectric-ferroelectric phase transition under axial tensile strain. Furthermore, the ground-state AFM order is predicted, and the emerging DMI effect, caused by strain-induced FE distortion, could alter the magnetic orientations from collinear configurations to non-collinear configurations. Both the FE polarizations and non-collinearity are monotonically increased with increasing strain. We further explore the shift current bulk photovoltaic effects (BPVE), which are recognized as the second-order nonlinear optical responses, under varying strains and different ferroelectric and magnetic states in the 1D WOI₃. The shift current is one of the direct BPVE photocurrents regained massive attention in both theoretical^{21–27} and experimental^{28–31} condensed matter physics due to its geometric nature and potential applications^{32–34}. It is noteworthy that the synthesis of bulk vdW WOI₃ has been reported decades ago³⁵. The 1D antiferroelectric (AFE) VOF₃, predicted to be a potential ultrahigh-energy-storage nanowire³⁶, shares the same structure, and the bulk vdW VOF₃ was also synthesized³⁷. Encouraged by the experimental achievements, this work suggests the 1D semiconductor WOI₃ as a promising multi-tunable platform for nonlinear optics, paving the way for next-generation devices that harness the intricate interplay of electricity and magnetism through nonlinear optical responses.

Results

Strain-induced ferroelectricity. We start with a brief description about the WOI_3 crystal in the paraelectric (PE) phase. The ladder-like 1D WOI_3 is formed by two 1D chains. Within the chains, highlighted in Fig. 1a, each tungsten (W) atom is confined in an irregular octahedron four planer iodine atoms (I) and two apical oxygen atoms (O). A $1 \times 1 \times 2$ cell of WOI_3 is used in DFT calculations (Fig. 1b). The crystal structure is built with inserting 17.2 \AA and 21.0 \AA vacuum layers over a and b directions, and is then optimized with a relaxed lattice constant $c = 3.825 \text{ \AA}$ in GGA-level accuracies. The PE structure of WOI_3 is in the space groups $Pmmm$ (No. 47) with two W atoms residing in the plane composed of the six planar I atoms. The structure of vdW bulk WOI_3 is presented in Fig. S1a. The calculated energy of extracting 1D WOI_3 wires from the bulk WOI_3 is approximately 25 meV/atom (Fig. S1b), implying experimental feasibility for exfoliation, akin to the exfoliation energy ($\sim 52 \text{ meV/atom}$) of a 2D graphene sheet.

Applying uniaxial tensile strain ε , the WOI_3 crystal demonstrates the capability to undergo a PE-to-FE structural phase transition. The nudged elastic band (NEB) calculations^{38,39} under $\varepsilon = 3\%$ yield two adiabatic energy pathways, and the results show that the structure in the FE/FE_{anti} phase is in the ground state (Fig. 1c), while the AFE/AFE_{anti} structure is metastable (Fig. 1d). The former belongs to $Pmm2$ (No. 25) space group with W^{5+} ions for both chains shifting along the same c direction, and the latter is in $Pm/2$ (No. 31) space group with cancelled polarization due to opposite c -direction displacements of W^{5+} . The energy barrier of reversing the FE polarizations in WOI_3 typically ranges in order of several dozens of meV/u.c.. Specifically, the barrier of PE state is 31.2 meV/u.c. and barrier between FE and AFE is 16.2 meV/u.c. under strain of $\varepsilon = 3\%$ (Figs. 1c-d). Compared with other low-dimensional materials, like 2D α - In_2Se_3 ($\sim 850 \text{ meV/u.c.}$)⁴⁰, the FE switching in WOI_3 can be easily achieved by applying electric fields.

For varying strain intensity ε , the transitions between PE, AFE and FE phases are elucidated by examining the energy differences, $\Delta E = E - E_{\text{PE},0\%}$ (depicted in Fig. 1e and summarized in Tab. 1) along with the specific angle α (Tab. 1). Here, the angle α refers to the angle at lower left corner of the cage shown in Fig. 1b. In the PE state under increasing intensity of strain ε , both ΔE_{PE} and α_{PE} become larger. Under strains of $2\% \leq \varepsilon \leq 5\%$, the differences between ΔE_{FE} (ΔE_{AFE}) and ΔE_{PE} are significant, and the FE state becomes the lowest-energy state with ΔE_{FE} being smaller than ΔE_{AFE} by a few meV. Regarding structural distortion, α_{FE} for FE state are consistently smaller than α_{PE} , while α_{AFE} for AFE state are larger than α_{PE} . With increasing strength of strains, the differences in angles become larger. However, for strains $\varepsilon < 1.8\%$, both α and ΔE of FE, AFE, and PE structures exhibit virtually no difference, which indicates that the PE-to-FE critical point (CP) may locate near strain $\varepsilon = 1.8\%$. The phase transition is further evident in the FE polarizations depicted in Fig. 1f, which increases monotonically above the CP strain and vanishes below it.

Anisotropic d^1 mechanism. The emergence of ferroelectricity in the strained 1D WOI_3 material could be attributed to the anisotropic d^1 rule. This rule has been recently introduced to elucidate potential multiferroic properties in 2D VOX_2 (X=Cl, Br, I) monolayer. Analysis of spatial charge densities and projected densities of states (PDOS) are conducted, as detailed in References¹⁴⁻¹⁶. Due

to an unpair d electron of W^{5+} centered at each octahedron, the WOI_3 is a non- d^0 system. We substantiate the applicability of the anisotropic d^1 rule for the strain-induced FE transition in WOI_3 by examining the charge density (Fig. 2a) and the PDOS (Figs. 2b and S3-S5). The xy -coordinates are clearly marked in Fig. 2a, and additional information regarding the selected xy -coordinates and spin polarizations can be found in Supplementary Note 1 and Fig. S2. The degree of coupling between W d -orbital and the O p -orbital is elucidated from the spin-polarized PDOS of ($\varepsilon = 0\%$, PE), ($\varepsilon = 3\%$, PE & FE), and ($\varepsilon = 5\%$, PE & FE) (Figs. S3-S5). With a discernible level of hybridization for $d_{xz}(d_{yz})$ -orbitals and O p -orbital, the coupling between d_{xy} -orbital and the O p -orbital remains negligible. The unpaired electrons occupying the d_{xy} -orbital (Fig. 2a) do not cause significant hindrance when W^{5+} moves along the W-O chain. On the other hand, the spin multiplicity of HOMO and LUMO configurations is illustrated from the PDOS of spin-up unit cell (Fig. 2b). Near the Fermi energy, the spin-up PDOS of occupied d_{xy} orbital indicates the HOMO configuration as $(t_{1u})^6(d_{xy}\uparrow)^1$. The observable spin-down PDOS of unoccupied $d_{xz}(d_{yz})$ orbitals informs a possible configuration of $(t_{1u})^5(d_{xy}\uparrow)^1(d_{yz}\downarrow + d_{xz}\downarrow)^1$ for LUMO, which share the same spin multiplicity as HOMO.

With hindrance-free d_{xy} electrons and same spin multiplicities, the anisotropic d^1 configuration bears resemblance to the conventional d^0 configuration, and the HOMO and LUMO can hybridize under the displacement of W^{5+} along the W-O bonds leading finite vibronic couplings. In the pristine WOI_3 ($\varepsilon = 0\%$), the vibronic-coupling contribution (K_V) might be insufficient to overcome the lattice stiffness (K_0). When applying tensile strains ($\varepsilon > 1.8\%$) to elongate the W-O bonds, the reduction of the energy gap (Fig. 2b) indicates an augmentation in the HOMO-LUMO hybridization, along with the vibronic-coupling contribution $|K_V|$. When $|K_V|$ surpassing K_0 , as indicated by $K_0 + K_V < 0$, the structural instabilities may be induced, leading to distortions due to the Pseudo Jahn-Teller effect (PJTE). The HOMO states are eventually stabilized with an expanded HOMO-LUMO energy gap under the PJTE-induced distortions, as shown by the results of ($\varepsilon = 3\%$, FE) in Fig. 2b.

Strain-tuning noncollinear antiferromagnetism. Next, we turn to the magnetic property of WOI_3 arising from the extra unpaired d electrons of W^{5+} . To explore the influence from the strain-induced FE distortion onto ground-state magnetic configurations, we include spin-orbit couplings (SOC) in DFT calculations, and then conduct MC simulations (“Methods”) based on the effective Heisenberg model⁴¹.

In the Heisenberg model, effective magnetic moments of atoms are incorporated for the study of macroscopic magnetic order. Both the magnitudes and directional dependence of atomic magnetic moments are carefully checked as follows to ensure a rational modelling. The magnitude of magnetic moment of W^{5+} is approximately $1.10 \mu_B$, obtained by integrating spin charge density within the effective radius in VASP. The magnetic moments of I^- and O^{2-} range within $0.01\text{-}0.04 \mu_B$, varying with distance from W^{5+} . These values align with the expected magnetic moments, considering the presence of one extra unpaired d electron of W^{5+} and four spin pairings of I^- and O^{2-} , with small deviations due to covalent bonding. The magnetic moments remain consistent under different strain magnitude in our DFT calculations. According to the Mermin-Wagner theorem⁴², directional isotropy for spins causes strong fluctuations to prohibit spontaneous symmetry broken in one- and two- dimensional spin systems. In magnetic ordered materials, like CrSbSe_3 studied in

our previous work⁴³, magnetic anisotropy plays a key role in suppression of such spin fluctuations. To demonstrate magnetic anisotropy of WOI₃, we perform MAE calculations for 3D energy profile by rotating the atomic magnetic moments over entire space under $\varepsilon = 0\%$ (Fig. 3a), and maintain opposing magnetic moments in neighboring unit cells (labelled as AFM 1, see Fig. 3c). The substantial magnetic anisotropy of WOI₃ is evident from the MAE profile. Thus, within the Heisenberg model, the strength of magnetic moments localized at W sites is treated as constant, and magnetic anisotropy is considered. Additionally, we determine the energetically favorable easy axis by careful numerical examinations with an error tolerance of 0.01π in solid angle, which lies at an angle of 43.20° with respect to *a*-axis and 62.61° for *c*-axis. The hard axis stays at angles of $(230.40^\circ, 32.86^\circ)$. These spin orientations hold for various strains less than $\varepsilon = 10\%$, as confirmed by DFT calculations with the same error tolerance, demonstrating the stability of the easy axis orientation across different strains.

Based on the aforementioned insights, we introduce the general Heisenberg Hamiltonian

$$H = \sum_{i \neq j} \sum_{\alpha=(a,b,c)} [J_{i,j;\alpha} s_i^\alpha s_j^\alpha + d_{i,j;\alpha} (\mathbf{s}_i \times \mathbf{s}_j)^\alpha] + \sum_i \sum_{\alpha=(a,b)} D_{i;\alpha} (s_i^\alpha)^2, \quad (1)$$

governing the collective behavior of the fixed-strength magnetic moments at W⁵⁺ sites, denoted by $\mathbf{s}_i = \{s_i^\alpha\} (\alpha = a, b, c)$. The magnetic anisotropy is addressed by the subscript α for all the coefficients in Eq. (1), including single-ion anisotropy coefficient, $D_{i;\alpha=(a,b)}$. For the PE structure (space group *Pmmm*), the asymmetric DMI of magnetic moments of 1D WOI₃ is zero due to inversion symmetry. However, when strain $\varepsilon (> 1.8\%)$ is applied, the FE deformation leads inversion symmetry breaking. Within a unit cell, a mirror plane includes both W⁵⁺'s and transect the W-I₂-W structure along the *ac* plane. According to Moriya's rules^{44,45}, finite DMI could be expected for FE structure, with the DMI coefficient vector being along the *b*-direction, $d_{i,j;\alpha=b}$. To estimate the strain effect onto magnetic noncollinearity, the DMI term with $d_{i,j;\alpha}$, is included in Eq. (1) for each pairing sites of $\{i, j\}$. Here, $J_{i,j;\alpha}$ represents the anisotropic exchange coefficient. Reasonable simplifications and truncations are further introduced in Eq. (1) to make MC simulations numerically feasible. The subscript i of the single-ion anisotropy coefficients $D_{i;\alpha}$ is omitted by assuming homogeneity for all W⁵⁺ sites, and the coefficients are collectively denoted as \mathbf{D} . As shown in Fig. 3b, the nearest-neighboring (NN) terms of Eq. (1) are mainly considered with NN exchange coefficient vectors, $\{\mathbf{J}_1, \mathbf{J}_2\}$, and NN DMI coefficient vectors, $\{\mathbf{d}_1, \mathbf{d}_2\}$. An additional next-nearest-neighboring (NNN) exchange term with \mathbf{J}_3 is also included to account for the minority of longer-range terms.

The coefficients $\mathbf{J}_{k(=1,2,3)}$, $\mathbf{d}_{k(=1,2)}$, and \mathbf{D} are determined by six kinds of specific magnetic configurations (Fig. 3c). Among these configurations, there are four collinear configurations, including FM, AFM 1, AFM 2, and AFM 3. Two additional noncollinear configurations are with clockwise (CW) and anti-clockwise (ACW) orientations. The total energy from DFT calculations for the six configurations are listed with different magnetic anisotropy ($\alpha = a, b, c$) and different strains ε in Table S1. For each anisotropic direction α , the determination of $J_{k(=1,2,3);\alpha}$ and D_α involving the linear equations parameterized the vectors of $s_i^\alpha s_j^\alpha$ and $(s_i^\alpha)^2$ (first column in Table.

[S1](#)) and their corresponding DFT energies plugged into Eq. (1). The values of $\mathbf{d}_{k(=1,2)}$ are subsequently determined by solving linear equations built from the remaining two noncollinear configurations. The determination process is repeated for various strains ε ($\leq 10\%$). The NN parameters are listed in [Table. 2](#), and the results for \mathbf{J}_3 and \mathbf{D} can be found in [Table. S2](#). Given that the values of NNN \mathbf{J}_3 are approximately 2 orders of magnitude smaller than NN $\mathbf{J}_{k=1,2}$, the effects of exchange interactions from longer-than-NN sites are expected to be minor. Notably, $d_{2,b}$ is finite, while other NN DMI coefficients remain negligible under different strains ε ($\geq 3\%$), which agrees with the predictions from Moriya's rules.

For the collinear magnetic configuration under each strain ε , the AFM 1 configuration is suggested to be the lowest-energy magnetic order, due to the positive \mathbf{J}_1 and negative \mathbf{J}_2 . As the FE distortion intensifies, the enhancement of noncollinearity is implied from the increase of the DMI $d_{2,b}$. To manifest the impact of noncollinearity within the 1D crystal model, the MC simulations based on Eq. (1) are then conducted to investigate the ground-state noncollinear magnetic configurations. According to the simulation results, the parallel magnetic moment vectors in l -th unit cell within PE structure are expanded with an intersection angle, θ_l , along the a -direction under the effect of FE distortion (as schematically shown in [Fig. 3d](#)). The growing noncollinearity with increasing strain ε is quantitatively characterized by the statistical average angle, $\theta = \langle \theta_l \rangle$, which is listed in [Table. 2](#).

Summarizing the complex phase behaviors around the CP strain $\varepsilon = 1.8\%$, we present a semi-schematic phase diagram ([Fig. S6](#)) delineating FE, AFE and PE states. Each phase is highlighted by discernible differences in the structural distortion, the FE polarization, and the magnetic noncollinearity. It is essential to note that this phase diagram representation is just one of the several possible configurations. Establishing of a more accurate phase diagram would require sophisticated calculations and even experimental measurements, which lie beyond the scope of this work.

Strain-induced shift current BPVE. Finally, we demonstrate the nonlinear optical (NLO) responses, specifically the shift currents BPVE under varying strain ε and different ferroelectric and magnetic states for the 1D WOI_3 material. As depicted in the schematic diagram ([Fig. 4a](#)), these three key factors in tuning the shift current response can be utilized in the future 1D WOI_3 -based NLO devices.

The formulation of the NLO response for shift current is briefly summarized here, with detailed derivations available in Refs.^{21–24}. In this work, we focus on the z -direction shift current induced by z -polarized light, expressed as $J_{\text{sh};z} = 2\sigma^{z;zz}(\omega)E(\omega)E(-\omega)$, and the shift current conductivity $\sigma^{z;zz}(\omega)$ is formulated as follows

$$\sigma^{z;zz}(\omega) = -\frac{\pi e^3}{2\hbar} \int_{\text{BZ}} \left(\frac{dk}{2\pi} \right) \sum_{n,m} f_{nm} |r_{nm}|^2 R_{nm;z} [\delta(\omega_{nm} - \omega) + \delta(\omega_{mn} - \omega)]. \quad (2)$$

Here, the difference for the Dirac-Fermi distributions and energies between of bands n and m are denoted by f_{nm} and ω_{nm} , respectively, and the summation in Eq. (2) runs over pairs of valence and conduction bands. For each (n, m) bands, the dipole moment is given by the inter-band Berry connections, $r_{nm}(k) = i(1 - \delta_{nm})\langle n|\partial_k|m\rangle$, while the gauge invariant shift vector is defined as, $R_{nm;z}(k) = -\partial_k\phi_{nm}(k) + A_n(k) - A_m(k)$. The intra-band Berry connection of n band is denoted as $A_n = i\langle n|\partial_k|n\rangle$ and the phase ϕ_{nm} is defined as $r_{nm} = |r_{nm}|e^{i\phi_{nm}}$. Here, $|n\rangle$ and $|m\rangle$ denote the cell-periodic Bloch states.

Based on the calculations of Eq. (2), the impact from strain engineering and FE distortion on the shift current response is explored (Figs. 4b). While maintaining WOI_3 in the FE and collinear AFM 1 state, abbreviated as (FE, AFM 1), the calculations of $\sigma^{z;zz}$ have been performed under different strain conditions, specifically, $\varepsilon = 0\%$, 2% , 3% , and 5% (Fig. 4b). For concise comparison, the frequency axes of the $\sigma^{z;zz}$ are rescaled by subtracting of the bandgap energy, $\omega - \omega_{\text{gap}} \rightarrow \omega$, where $\omega_{\text{gap}} = 0.79$ eV, 0.88 eV, 1.02 eV, and 1.22 eV. Without any strain ($\varepsilon = 0\%$), the shift current response vanishes due to the inversion symmetry, though finite dipole leads to a finite linear optical response (Supplementary Note 2 and Fig. S7a). Within the frequency range of $\omega = [0, 0.6]$ eV, the overall profiles of oscillatory shift current responses become larger with increasing frequency for different finite strains, and the increasing trend can be also inspected in linear optical response (Fig. S7a). The enhancement in large frequencies is originated from the augmentation of transition strength $|r_{nm}(k)|^2$ among deep bands. As shown in the band structure (Fig. 5a) and k -resolved shift current response (Fig. 5c) under $\varepsilon = 3\%$, the near-gap shift current response mainly arise from the weak C_{2v} -symmetry-allowed transitions between the valence band maximum (VBM) featured with I p_z orbitals at Γ point and conduction band (I p_z and W $(d_{x'z} + d_{y'z})$ orbitals). When the light frequency increases, the results of k -resolved shift current response indicate that the pronounced transitions at k points of $\Gamma \rightarrow \pm Z$ gradually become the primary contribution (Fig. 5c), where the components of the flat valence bands turn to be W $d_{x'^2-y'^2}$ orbitals (Fig. 5a). Note that the $x'y'$ -coordinates are marked in Fig. 2a. As ε increases, the flat valence bands are lifted close to the VBM (Figs. S8-S11), and the profiles of the linear optical responses are brought forward (Fig. S7a). However, within the frequency range of $\omega = [0, 0.6]$ eV, the shift current response under $\varepsilon = 3\%$ emerges as an optimal choice, reaching a maximum of about $16 \text{ nm}^2 \cdot \mu\text{A}/\text{V}^2$ at rescaled frequency of $\omega_{\text{max}} = 0.47$ eV. When yielding comparable strength of shift current responses, ω_{max} 's of $\varepsilon = 2\%$ and 5% are larger than $\varepsilon = 3\%$. The effect of the FE distortion is then investigated from the shift current responses across changing ferroelectric states including results for PE, AFE, FE and FE_{anti} states under $\varepsilon = 3\%$ (Fig. 4b). Here, the magnetic configuration of WOI_3 consistently follows the collinear AFM 1 order. In the FE_{anti} state, flipping the direction of the FE polarization reverse the sign of $R_{nm;z}$, and the shift current response of FE_{anti} state is opposite from FE state. By contrast, the shift current responses of PE and AFE states vanish due to inversion symmetry. Applying strains and coercive fields can be utilized to act as on-off and directional switches for NLO based devices.

The influence of the magnetic properties to shift current response is then explored by changing the magnetic configurations while maintaining the 1D WOI_3 in the FE state under $\varepsilon = 3\%$. When transitioning collinear AFM 1 to FM phase, the near-gap shift current response $\sigma^{z;zz}$ is shifted to higher light frequency (Fig. 4d). This altering of response arises from the change in $|r_{nm}(k)|^2$, as supported by additional information from k -resolved shift current response (Fig. 5d) and linear optical response (Fig. S7b). The splitting of doubly degenerate bands noticeably reduces the

densities of states (DOS) of the gap-edge energy regions (Figs. 5a-b and S12), and optical selection rule dominates the suppression of transitions from the gap-edge valence band at the k points of the valleys of conduction bands (Figs. 5b). Both effects then diminish the gap-edge transitions $|r_{nm}(k)|^2$ for FM order leading the altering of shift current response. Additionally, the strain-induced magnetic noncollinearity is found to have negligible effect onto the shift current response (Fig. S13), while the changes for behaviors of shift current response are minor when altering the direction of the magnetic moments of WOI_3 from the easy axis to a axis. It aligns with expectation that changing magnetic orders is more pronounced than fine-tuning magnetic configurations on the electronic structures.

Discussions

In this work, we report theoretical investigations on the 1D vdW WOI_3 . A strain-induced paraelectric-ferroelectric phase transition is predicted with critical point of strain $\varepsilon_{\text{CP}} \sim 1.8\%$ for this material. Our calculations identify WOI_3 as a 1D ferroelectric-antiferromagnetic (multiferroic) semiconductor by strain engineering, where the magnetic moments are originated from the unpaired d_{xy} electrons in d^1 configuration of the tungsten atoms. The strain-induced FE distortions ($3\% \leq \varepsilon \leq 10\%$) can also lead $5^\circ \sim 12^\circ$ noncollinear tilting of the magnetic moments, pristinely parallel to the easy axis ($\varepsilon = 0\%$), along the direction of the FE polarization. Subsequently, we explore the ferroelectric and magnetic properties concerning shift current BPVE in 1D WOI_3 . Strains and electric fields serve as efficient controls for on-off and direction-switching of NLO responses. Additionally, changing the magnetic order has been identified as a way to manipulate NLO responses. These pave the way for the design of advanced optical devices with tailored properties.

We rationalize the multiferroicity in 1D vdW WOI_3 from the anisotropic d^1 rule, as proposed in works of 2D VOX_2 (X=Cl, Br, I)^{14,15}. The scarcity of systematic investigations into the anisotropic d^1 rule in generating FE distortion and its implications in designing novel electromagnetic materials remains a significant gap in our understanding. This work sheds light on the discovery of new anisotropic d^1 materials, offering insights for the theoretical development of the anisotropic d^1 rule. Furthermore, 1D vdW WOI_3 is expected to be a multi-tune platform for devices utilizing shift current BPVE. The efficient control of shift current through the application of strains, external electric fields, and magnetic field is promising for potential applications in NLO devices. Due to the success in synthesis of the bulk vdW WOI_3 ³⁵ and VOF_3 ³⁷, experimental verifications and applications in NLO devices could be achieved for the foreseeable future.

Methods

Computational details. Density functional theory (DFT)^{46,47} calculations are performed by Vienna *Ab initio* Simulation Package (VASP)^{48,49}, which employs projected augmented-wave (PAW) approach for the core electrons. The generalized gradient approximated (GGA) functionals^{50,51} of Perdew-Burke-Ernzerhof (PBE) type parameterization⁵² are implemented to consider the exchange-correlation energy of all valence electrons. Due to strong electronic localization for 5d electrons of W atoms, the Hubbard correction with simplification of Dudarev *et. al*⁵³ is further added to the GGA functionals with parameters, $U_{\text{eff}} = U - J = 2$ eV. The $1 \times 1 \times 2$ supercell of 1D WOI₃ material is mainly used in DFT calculations, allowing for six different magnetic configurations being taken into account. A cutoff energy for the plane-wave basis sets is set to 450 eV, and a $1 \times 1 \times 7$ k point sampling is used. The DFT results are consistently obtained under the convergence criteria of 0.01 eV/Å and 1×10^{-6} eV for residual forces in ion relaxations and energy difference between successive self-consistent field (SCF) calculation steps, respectively.

Based on DFT calculations, ferroelectric and magnetic properties of WOI₃ are further explored through following methods. The standard Berry phase approach⁵⁴ is performed to calculate FE polarizations. The torque method^{55,56} is applied for magnetic anisotropy energy (MAE) profile with an error tolerance of $\sim 0.01\pi$ solid angle. In the Monte Carlo (MC) simulations of the Heisenberg model for WOI₃, the orientations of magnetic moment are sampled in a supercell of $1 \times 1 \times 2000$ grids to get rid of interference from the boundaries. Simulations are performed under a temperature of 10^{-8} K, and the MC Metropolis algorithm⁵⁷ and the Hinzke-Nowak methods⁵⁸ are introduced to improving the sampling efficiency. Initial magnetic configurations are deployed randomly, and a dynamic balance of the magnetic moments is reached after 1×10^5 steps.

The Wannier-interpolation scheme^{59,60} is employed in calculations for shift current responses. The maximally-localized Wannier functions (MLWF) are obtained iteratively with initial guess constructed by projection functions of W *d*-, I *p*-, and O *p*-orbitals, as implemented in the Wannier90 code⁶¹. The tight-binding model is built from the basis set of MLWF, and the Wannier Berri code⁶² is then performed to calculate the shift current response. Within the calculations, a dense k -point mesh of $1 \times 1 \times 400$ for integrations and a fixed width of 0.025 eV for broadening Dirac δ -functions are adapted.

The visualization of the crystal structures are carried out by VESTA software⁶³. The output data from above codes are in units of 3D systems. The 1D results for shift current response ($\text{nm}^2 \cdot \mu\text{A}/\text{V}^2$), linear optical response ($\text{pS} \cdot \text{cm}$), and FE polarization ($\text{pC} \cdot \text{m}$) are then obtained by multiplying data with the cross section of 25 Å \times 25 Å.

REFERENCES

1. Khomskii, D. I. Multiferroics: Different ways to combine magnetism and ferroelectricity. *J. Magn. Magn. Mater.* **306**, 1–8 (2006).
2. Khomskii, D. Classifying multiferroics: Mechanisms and effects. *Physics* **2**, 20 (2009).
3. Fiebig, M., Lottermoser, T., Meier, D. & Trassin, M. The evolution of multiferroics. *Nat. Rev. Mater.* **1**, 16046 (2016).
4. Spaldin, N. A. & Ramesh, R. Advances in magnetoelectric multiferroics. *Nature Mater.* **18**, 203–212 (2019).
5. Hu, T. & Kan, E. Progress and prospects in low-dimensional multiferroic materials. *Wiley Interdiscip. Rev. Comput. Mol. Sci.* **9**, e1409 (2019).
6. Tang, X. & Kou, L. Two-Dimensional Ferroics and Multiferroics: Platforms for New Physics and Applications. *J. Phys. Chem. Lett.* **10**, 6634–6649 (2019).
7. Yang, Q., Xiong, W., Zhu, L., Gao, G. & Wu, M. Chemically Functionalized Phosphorene: Two-Dimensional Multiferroics with Vertical Polarization and Mobile Magnetism. *J. Am. Chem. Soc.* **139**, 11506–11512 (2017).
8. Lu, Y. *et al.* Artificial Multiferroics and Enhanced Magnetoelectric Effect in van der Waals Heterostructures. *ACS Appl. Mater. Interfaces* **12**, 6243–6249 (2020).
9. Huang, C. *et al.* Prediction of Intrinsic Ferromagnetic Ferroelectricity in a Transition-Metal Halide Monolayer. *Phys. Rev. Lett.* **120**, 147601 (2018).
10. Zhang, J.-J. *et al.* Type-II Multiferroic $\text{Hf}_2\text{VC}_2\text{F}_2$ MXene Monolayer with High Transition Temperature. *J. Am. Chem. Soc.* **140**, 9768–9773 (2018).
11. Ju, H. *et al.* Possible Persistence of Multiferroic Order down to Bilayer Limit of van der Waals Material NiI_2 . *Nano Lett.* **21**, 5126–5132 (2021).
12. Guo, J. W. *et al.* Strain-induced ferroelectricity and spin-lattice coupling in SrMnO_3 thin films. *Phys. Rev. B* **97**, 235135 (2018).
13. Sakai, H. *et al.* Displacement-Type Ferroelectricity with Off-Center Magnetic Ions in Perovskite $\text{Sr}_{1-x}\text{Ba}_x\text{MnO}_3$. *Phys. Rev. Lett.* **107**, 137601 (2011).
14. Tan, H. *et al.* Two-dimensional ferromagnetic-ferroelectric multiferroics in violation of the d^0 rule. *Phys. Rev. B* **99**, 195434 (2019).
15. Ai, H., Song, X., Qi, S., Li, W. & Zhao, M. Intrinsic multiferroicity in two-dimensional VOCl_2 monolayers. *Nanoscale* **11**, 1103–1110 (2019).
16. Ding, N., Chen, J., Dong, S. & Stroppa, A. Ferroelectricity and ferromagnetism in a VOI_2

monolayer: Role of the Dzyaloshinskii-Moriya interaction. *Phys. Rev. B* **102**, 165129 (2020).

17. Bersuker, I. B. Pseudo Jahn-Teller Origin of Perovskite Multiferroics, Magnetic-Ferroelectric Crossover, and Magnetoelectric Effects: The d^0 – d^{10} Problem. *Phys. Rev. Lett.* **108**, 137202 (2012).
18. Bersuker, I. B. *The Jahn-Teller effect*. (Cambridge University Press, 2010).
19. Lin, L.-F., Zhang, Y., Moreo, A., Dagotto, E. & Dong, S. Quasi-one-dimensional ferroelectricity and piezoelectricity in WO_4 halogens. *Phys. Rev. Mater.* **3**, 111401 (2019).
20. Xu, T. *et al.* Intrinsic ferroelectrics and carrier doping-induced metallic multiferroics in an atomic wire. *J. Mater.* **9**, 892–898 (2023).
21. von Baltz, R. & Kraut, W. Theory of the bulk photovoltaic effect in pure crystals. *Phys. Rev. B* **23**, 5590–5596 (1981).
22. Sturman, B. I. & Fridkin, V. M. *Photovoltaic and photo-refractive effects in noncentrosymmetric materials*. (Routledge, 2021).
23. Sipe, J. E. & Shkrebttii, A. I. Second-order optical response in semiconductors. *Phys. Rev. B* **61**, 5337–5352 (2000).
24. Young, S. M. & Rappe, A. M. First Principles Calculation of the Shift Current Photovoltaic Effect in Ferroelectrics. *Phys. Rev. Lett.* **109**, 116601 (2012).
25. Strasser, A., Wang, H. & Qian, X. Nonlinear Optical and Photocurrent Responses in Janus MoS₂ Monolayer and MoS₂–MoS₂ van der Waals Heterostructure. *Nano Lett.* **22**, 4145–4152 (2022).
26. Wang, H., Tang, X., Xu, H., Li, J. & Qian, X. Generalized Wilson loop method for nonlinear light-matter interaction. *npj Quantum Mater.* **7**, 61 (2022).
27. Cook, A. M., M. Fregoso, B., de Juan, F., Coh, S. & Moore, J. E. Design principles for shift current photovoltaics. *Nat. Commun.* **8**, 14176 (2017).
28. Nakamura, M. *et al.* Shift current photovoltaic effect in a ferroelectric charge-transfer complex. *Nat. Commun.* **8**, 281 (2017).
29. Ma, J. *et al.* Nonlinear photoresponse of type-II Weyl semimetals. *Nat. Mater.* **18**, 476–481 (2019).
30. Burger, A. M. *et al.* Direct observation of shift and ballistic photovoltaic currents. *Sci. Adv.* **5**, eaau5588 (2019).
31. Hatada, H. *et al.* Defect tolerant zero-bias topological photocurrent in a ferroelectric semiconductor. *Proc. Natl. Acad. Sci. U. S. A.* **117**, 20411–20415 (2020).
32. Tan, L. Z. *et al.* Shift current bulk photovoltaic effect in polar materials–hybrid and oxide perovskites and beyond. *npj Comput Mater.* **2**, 16026 (2016).

33. Zhou, Y. *et al.* Nonlinear optical properties of halide perovskites and their applications. *Appl. Phys. Rev.* **7**, 041313 (2020).
34. Dang, Y. & Tao, X. Recent progress of bulk photovoltaic effect in acentric single crystals and optoelectronic devices. *Matter* **5**, 2659–2684 (2022).
35. Krebs, B., Brendel, C. & Schäfer, H. Über die Reaktion von W_3O mit Iod. Darstellung, Kristallstruktur und Eigenschaften von WOI_3 . *Z. Anorg. Allg. Chem.* **553**, 127–135 (1987).
36. Xu, T., Zhang, J., Shimada, T., Wang, J. & Yang, H. Intrinsic Atomic-Scale Antiferroelectric VOF_3 Nanowire with Ultrahigh-Energy Storage Properties. *Nano Lett.* **23**, 9080–9086 (2023).
37. Selig, H. & Claassen, H. H. Infrared Spectra of VOF_3 and POF_3 . *J. Chem. Phys.* **44**, 1404–1406 (1966).
38. Mills, G., Jónsson, H. & Schenter, G. K. Reversible work transition state theory: application to dissociative adsorption of hydrogen. *Surf. Sci.* **324**, 305–337 (1995).
39. Berne, B. J., Ciccotti, G. & Coker, D. F. Nudged elastic band method for finding minimum energy paths of transitions. in *Classical and Quantum Dynamics in Condensed Phase Simulations* (World Scientific, 1998).
40. Ding, W. *et al.* Prediction of intrinsic two-dimensional ferroelectrics in In_2Se_3 and other III₂-VI₃ van der Waals materials. *Nat. Commun.* **8**, 14956 (2017).
41. Lado, J. L. & Fernández-Rossier, J. On the origin of magnetic anisotropy in two dimensional CrI_3 . *2D Mater.* **4**, 035002 (2017).
42. Mermin, N. D. & Wagner, H. Absence of Ferromagnetism or Antiferromagnetism in One- or Two-Dimensional Isotropic Heisenberg Models. *Phys. Rev. Lett.* **17**, 1133–1136 (1966).
43. Xun, Y., Zhu, Z., Chen, X. & Qi, J. One-dimensional ferromagnetic semiconductor $CrSbSe_3$ with high Curie temperature and large magnetic anisotropy. *Phys. Rev. B* **104**, 085429 (2021).
44. Dong, S., Xiang, H. & Dagotto, E. Magnetoelectricity in multiferroics: a theoretical perspective. *Natl. Sci. Rev.* **6**, 629–641 (2019).
45. Moriya, T. New Mechanism of Anisotropic Superexchange Interaction. *Phys. Rev. Lett.* **4**, 228–230 (1960).
46. Hohenberg, P. & Kohn, W. Inhomogeneous Electron Gas. *Phys. Rev.* **136**, B864–B871 (1964).
47. Kohn, W. & Sham, L. J. Self-Consistent Equations Including Exchange and Correlation Effects. *Phys. Rev.* **140**, A1133–A1138 (1965).
48. Kresse, G. & Hafner, J. *Ab initio* molecular dynamics for liquid metals. *Phys. Rev. B* **47**, 558–561 (1993).
49. Kresse, G. & Furthmüller, J. Efficiency of ab-initio total energy calculations for metals and

semiconductors using a plane-wave basis set. *Comput. Mater. Sci.* **6**, 15–50 (1996).

50. Becke, A. D. Density-functional exchange-energy approximation with correct asymptotic behavior. *Phys. Rev. A* **38**, 3098–3100 (1988).
51. Langreth, D. C. & Mehl, M. J. Beyond the local-density approximation in calculations of ground-state electronic properties. *Phys. Rev. B* **28**, 1809–1834 (1983).
52. Perdew, J. P., Burke, K. & Ernzerhof, M. Generalized Gradient Approximation Made Simple. *Phys. Rev. Lett.* **77**, 3865–3868 (1996).
53. Dudarev, S. L., Botton, G. A., Savrasov, S. Y., Humphreys, C. J. & Sutton, A. P. Electron-energy-loss spectra and the structural stability of nickel oxide: An LSDA+U study. *Phys. Rev. B* **57**, 1505–1509 (1998).
54. King-Smith, R. D. & Vanderbilt, D. Theory of polarization of crystalline solids. *Phys. Rev. B* **47**, 1651–1654 (1993).
55. Wang, X., Wu, R., Wang, D. & Freeman, A. J. Torque method for the theoretical determination of magnetocrystalline anisotropy. *Phys. Rev. B* **54**, 61–64 (1996).
56. Wu, R. & Freeman, A. J. Spin–orbit induced magnetic phenomena in bulk metals and their surfaces and interfaces. *J. Magn. Magn. Mater.* **200**, 498–514 (1999).
57. Metropolis, N., Rosenbluth, A. W., Rosenbluth, M. N., Teller, A. H. & Teller, E. Equation of State Calculations by Fast Computing Machines. *J. Chem. Phys.* **21**, 1087–1092 (1953).
58. Hinzke, D. & Nowak, U. Magnetization switching in a Heisenberg model for small ferromagnetic particles. *Phys. Rev. B* **58**, 265–272 (1998).
59. Ibañez-Azpiroz, J., Tsirkin, S. S. & Souza, I. Ab initio calculation of the shift photocurrent by Wannier interpolation. *Phys. Rev. B* **97**, 245143 (2018).
60. Marzari, N., Mostofi, A. A., Yates, J. R., Souza, I. & Vanderbilt, D. Maximally localized Wannier functions: Theory and applications. *Rev. Mod. Phys.* **84**, 1419–1475 (2012).
61. Pizzi, G. *et al.* Wannier90 as a community code: new features and applications. *J. Phys.: Condens. Matter* **32**, 165902 (2020).
62. Tsirkin, S. S. High performance Wannier interpolation of Berry curvature and related quantities with WannierBerri code. *npj Comput. Mater.* **7**, 33 (2021).
63. Momma, K. & Izumi, F. *VESTA 3* for three-dimensional visualization of crystal, volumetric and morphology data. *J. Appl. Cryst.* **44**, 1272–1276 (2011).

ACKNOWLEDGEMENTS

H. W. and J. Q. acknowledge the support provided by National Natural Science Foundation of China (NSFC) under Grant No. 12304049 and 11974148. The work was carried out at National Supercomputer Center in Tianjin, and the calculations were performed on TianHe-1(A). Z. G. acknowledges Prof. Mingwen Zhao and Mr. Haoqiang Ai for useful discussions.

AUTHOR CONTRIBUTIONS

H. W. and J. Q. conceived the idea. Z. G. and Y. X. performed the calculations and wrote the paper with the help of H. W. and J. Q. All authors analyzed the data, contributed to the discussions of the results and revised the manuscript.

COMPETING INTERESTS

The authors declare no competing financial interests.

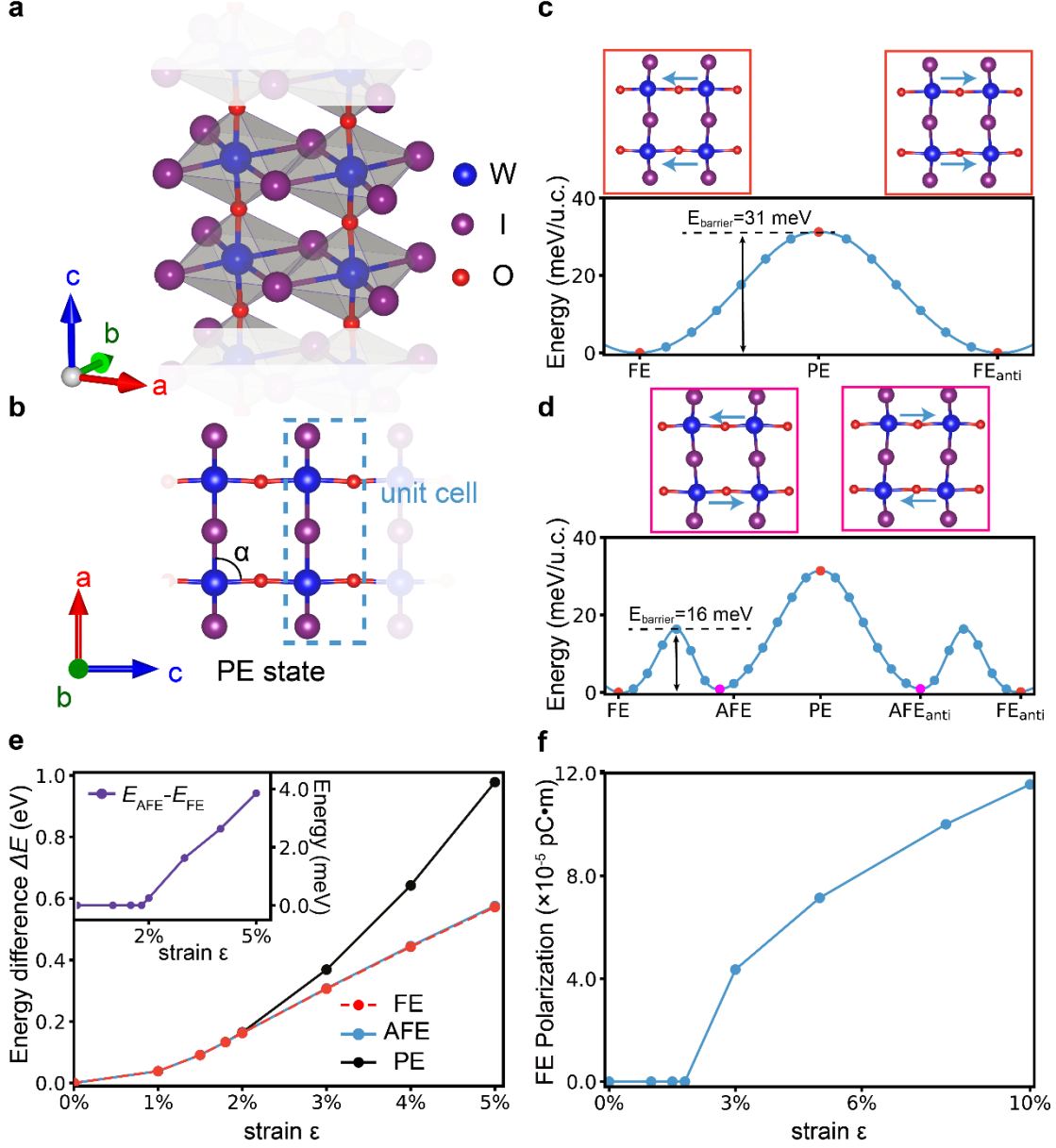


Figure 1. Crystal structures and Ferroelectricity for the 1D WOI_3 . The structures of PE state viewed in (a) the crystal orientation and in (b) the b -direction. The rung-like unit cell is highlighted in the blue dashed box, and the specific O–W–I bond angle α in lower left corner of the cage of the $1 \times 1 \times 2$ cell characterizes the distortion degree. Under a uniaxial strain of $\epsilon = 3\%$, the adiabatic energy pathways from the nudged elastic band (neb) are presented for (c) FE-PE-FE_{anti} and (d) FE-AFE-PE-AFE_{anti}-FE_{anti}, with structures of the FE/FE_{anti} and AFE/AFE_{anti} states addressed. Here, the energy barriers of transition states are labelled. The FE_{anti} represent the FE state with the opposite polarization direction. (e) The energy difference $\Delta E = E - E_{\text{PE},0\%}$ of different state under $\epsilon = 0\%-5\%$, and the energy difference between FE and AFE is presented in the inserted figure. (f) The FE polarization intensity along the periodic direction c -axis P_c under different strains.

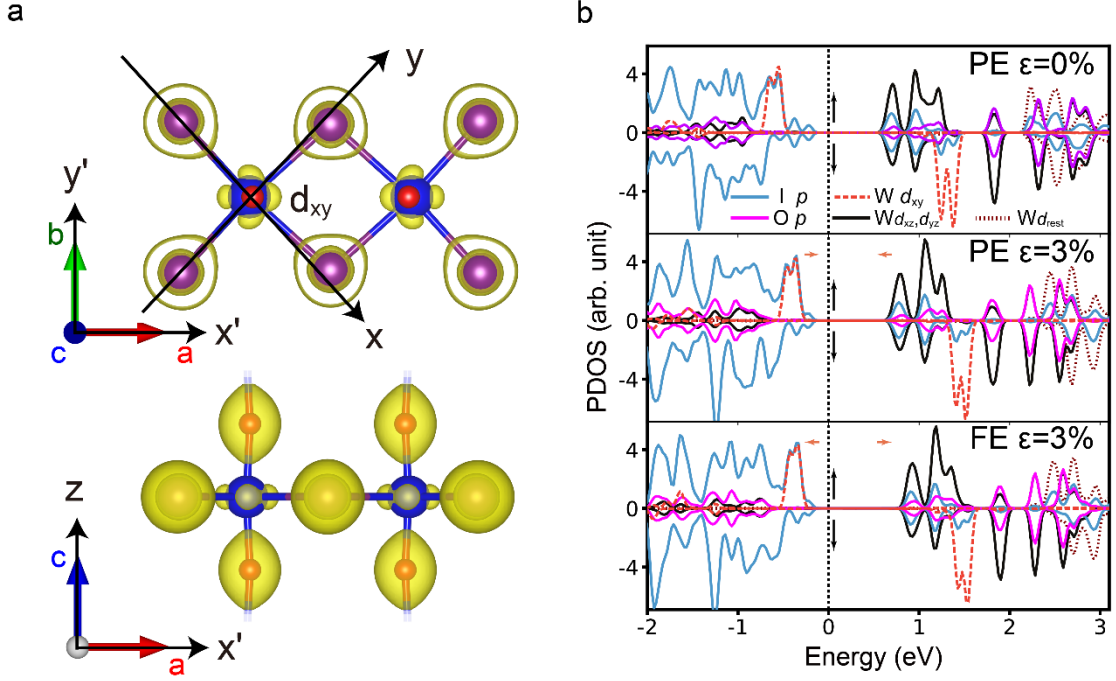


Figure 2. Spatial charge densities and spin-polarized PDOS in supporting the ferroelectric anisotropic d^1 rule. (a) The charge densities represented by yellow isosurfaces with isosurface level of 0.09 e/Bohr^3 . The charge densities localized at W atoms correspond to the occupied d_{xy} orbitals. Here, the xy -coordination axes for the orbitals are set to be aligned with the I-W bonds, distinguished from the marked $x'y'$ -coordination axes. (b) The spin-up and spin-down PDOS for ($\epsilon = 0\%$, PE), ($\epsilon = 3\%$, PE), and ($\epsilon = 3\%$, FE) are presented within the near-gap energy region. The red dashed and black solid lines represent the PDOS of d_{xy} and $d_{xz} + d_{yz}$ orbitals for W atoms, while the brown dotted lines are PDOS for rest orbitals of W atoms. The p orbitals of I and O atoms are respectively denoted by blue and magenta solid lines.

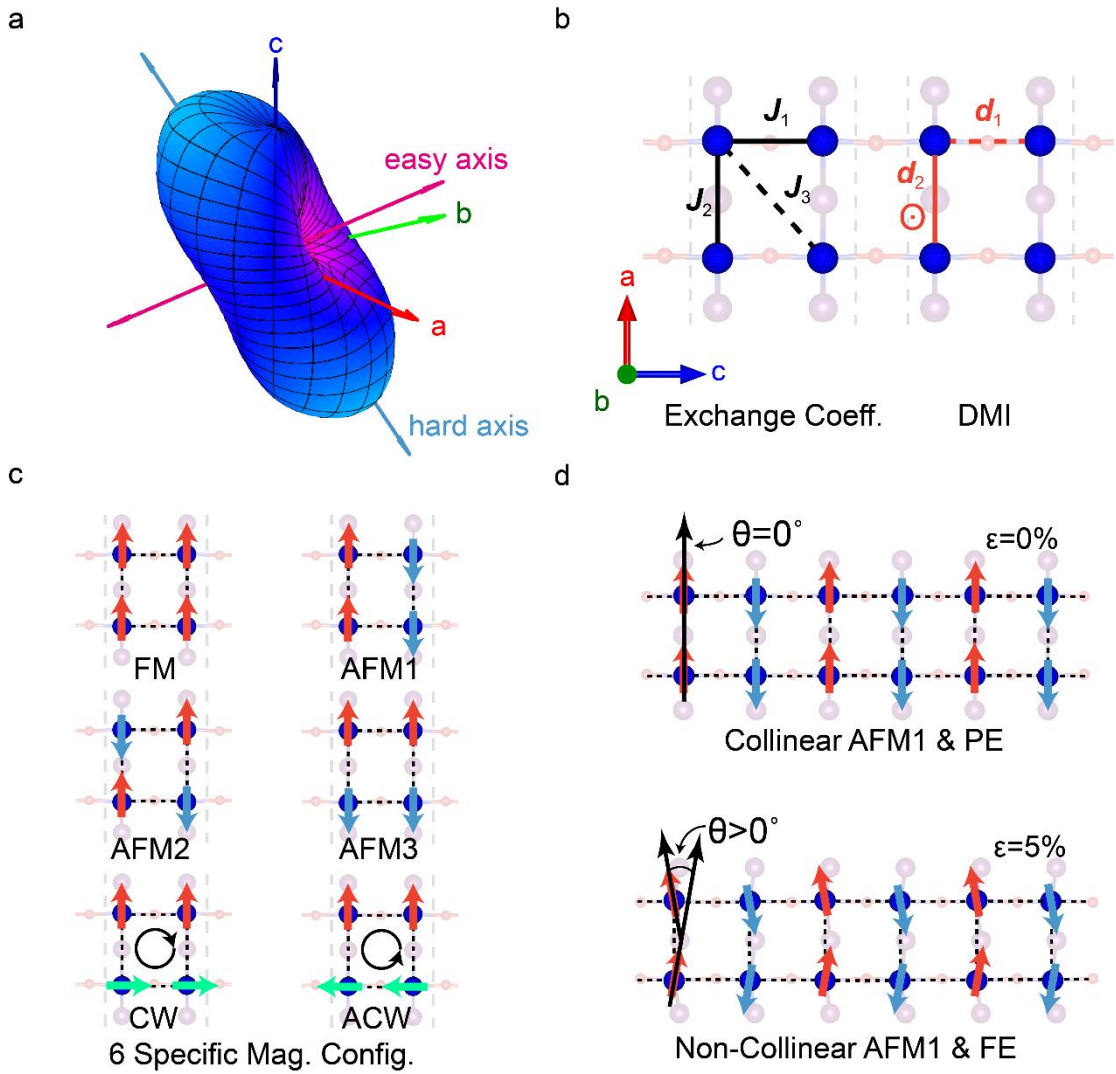


Figure 3. MAE surface and schematics of Heisenberg models and magnetic configurations.

(a) The MAE surface of the 1D WOI_3 with easy axis (red) and hard axis (blue). (b) The schematic diagrams for the exchange coefficients and DMI vectors considered in the anisotropic Heisenberg model. (c) six specific magnetic configurations used in determining parameters of the anisotropic Heisenberg model. These configurations are collinear Ferromagnetic (FM) order and three kinds of Antiferromagnetic (AFM 1-3) orders, and non-collinear Clockwise (CW) and Anticlockwise (ACW) configurations. (d) Schematic diagrams for the magnetic configurations under strain of $\varepsilon=0\%$ and $\varepsilon=5\%$. The red and blue represent the magnetic moments at sites of W atom in a rung-like unit cell, and the averaged intersection angle θ is introduced to characterize the degrees of the noncollinearity.

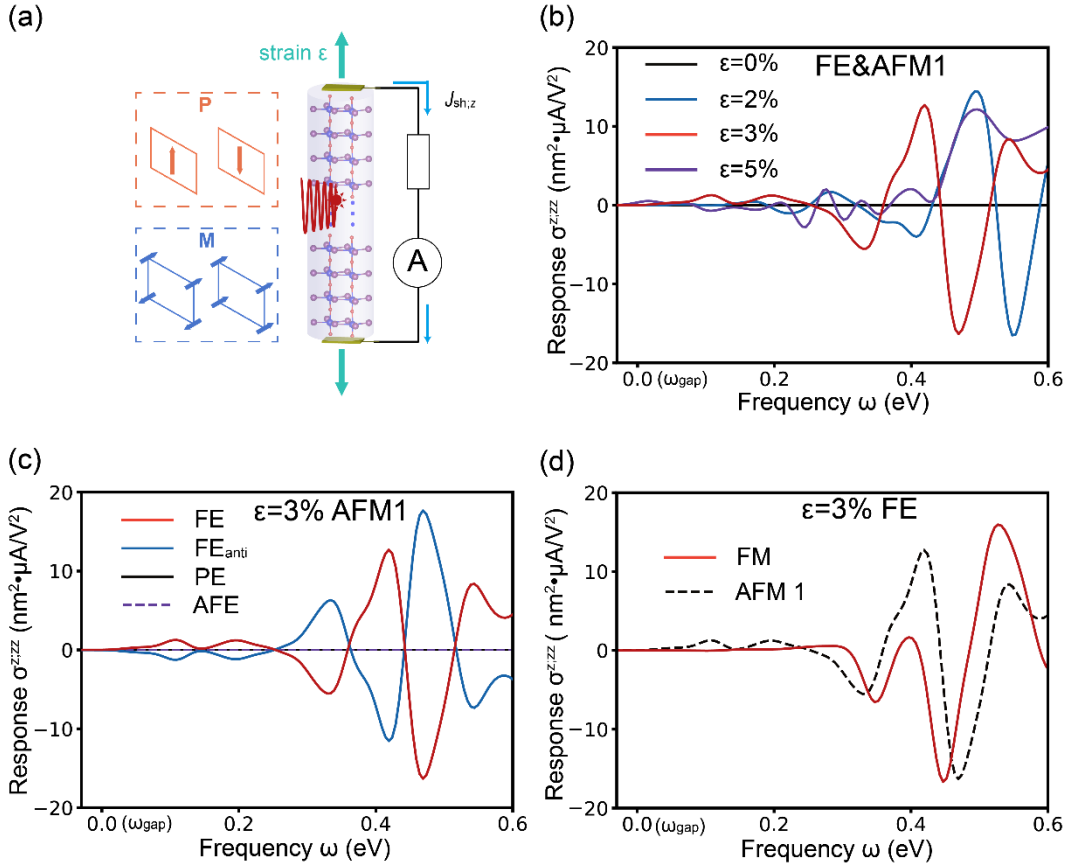


Figure 4. Shift current response for 1D WOI₃. (a) The schematic diagram for the WOI₃-based NLO device. The shift current responses $\sigma^{z,zz}(\omega)$ for (b) (FE, AFM 1) state under $\epsilon = 0\%$, 2%, 3%, and 5% represented by black, blue, red and purple lines; (c) FE, FE_{anti}, PE, and AFE structure with AFM 1 under $\epsilon = 3\%$ represented by red, blue, black solid and purple dashed lines; (d) FE structure with AFM 1 and FM phases under $\epsilon = 3\%$ denoted by black dashed and red solid lines. The collinear magnetic orientation is along with easy axis in (b)-(d).

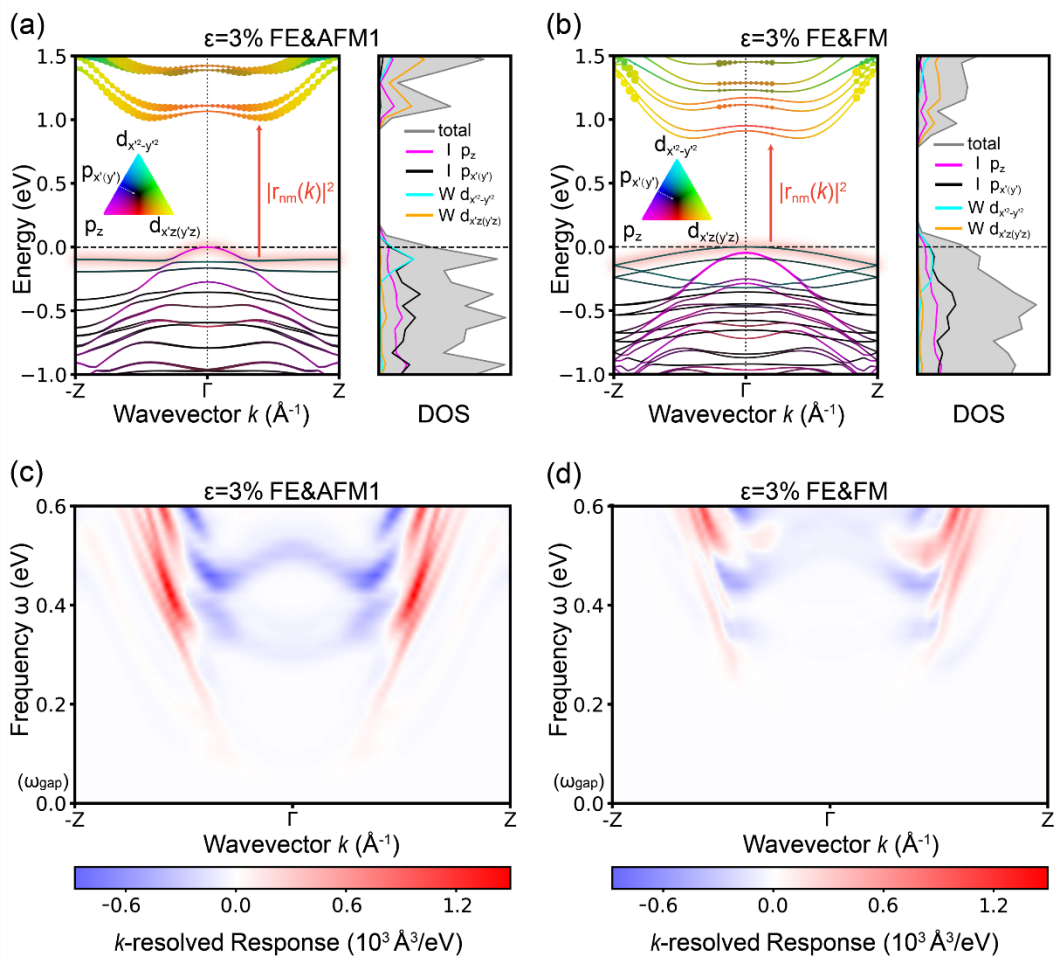


Figure 5. Band structures and k -resolved shift current response for 1D WOI_3 . The band structures and densities of states (DOS) of (a) (FE, AFM 1) and (b) (FE, FM) states under $\varepsilon = 3\%$. The color composition for each point of orbital projection in bands, using colors (yellow, cyan, black, and magenta), indicates the proportions of $\text{W } d_{x'z} + d_{y'z}$, $\text{W } d_{x'^2-y'^2}$, $\text{I } p_x + p_y$, and $\text{I } p_z$ orbitals. The sizes of solid circles represent the strength of transition dipole moments, $|r_{nm}(k)|^2$, from first gap-edge valence band to conduction bands. The total DOS and orbital PDOS are denoted by grey shaded line and colored lines, respectively. The k -resolved shift current responses of (c) (FE, AFM 1) and (d) (FE, FM) states under $\varepsilon = 3\%$ are plotted with k points and light frequencies.

STRAIN	ΔE (eV)			α (°)			
	ε	PE	FE	AFE	PE	FE	AFE
0%		0	–	–	88.0972	–	–
1%	0.038583	0.038583	0.038583	88.1990	88.2007	88.2046	
1.5%	0.091284	0.091285	0.091288	88.2475	88.2120	88.2250	
1.8%	0.132926	0.132926	0.132927	88.2725	88.2360	88.2506	
2%	0.164657	0.162495	0.162743	88.2942	86.8346	89.6263	
3%	0.368723	0.306299	0.307929	88.4168	84.7014	91.5060	
4%	0.642511	0.442843	0.445473	88.4168	83.7014	92.6567	
5%	0.978206	0.571920	0.575775	88.4676	82.7923	93.5199	

Table 1. The energy difference, $\Delta E = E - E_{\text{PE,0\%}}$, (left panel) and the angle, α , characterizing the magnitude of structure distortion (right panel) for PE, FE, and AFE states under strain $\varepsilon = 0\%$ to 5%.

STRAIN ε	J_1	J_2	$d_{2;a=b}$	θ (°)
	(meV/ μ_B^2)			
0%	<i>a</i> :	1.07(2)	−4.28(8)	0
	<i>b</i> :	0.79(4)	−4.50(9)	
	<i>c</i> :	1.18(6)	−4.44(5)	
3%	<i>a</i> :	0.85(9)	−3.98(1)	0.49 (5)
	<i>b</i> :	0.63(9)	−3.81(5)	
	<i>c</i> :	0.95(6)	−4.13(2)	
5%	<i>a</i> :	0.72(5)	−3.77(3)	0.62(3)
	<i>b</i> :	0.60(5)	−3.15(9)	
	<i>c</i> :	0.77(4)	−3.92(6)	
8%	<i>a</i> :	0.49(8)	−3.57(7)	0.91(9)
	<i>b</i> :	0.45(8)	−2.66(8)	
	<i>c</i> :	0.51(1)	−3.75(7)	
10%	<i>a</i> :	0.40(4)	−3.58(3)	0.98(0)
	<i>b</i> :	0.37(1)	−2.59(6)	
	<i>c</i> :	0.41(5)	−3.76(9)	

Table 2. The results of NN exchange coefficients and DMI, J_1, J_2 , and $d_{2;b}$, for the anisotropic Heisenberg model and the averaged intersection angle θ under strains of $\varepsilon = 0\%$ to 10% .